JOURNAL OF GEOPHYSICAL RESEARCH, VOL. 87, NO. B5, PAGES 3949–3958, MAY 10, 1982

Geoid Height-Age Relation From SEASAT Altimeter Profiles Across the Mendocino Fracture Zone

DAVID T. SANDWELL[1] AND GERALD SCHUBERT

Department of Earth and Space Sciences, University of California, Los Angeles, California 90024

Twenty-eight SEASAT altimeter profiles crossing the Mendocino Fracture Zone are used together with seafloor ages determined from magnetic lineations to estimate the change in oceanic geoid height with age, between ages of 15 and 135 m.y. An unbiased estimate of the overall geoid offset along each profile is determined from a least-squares fit of the along-track derivative of the geoid to the geoid slope predicted from a simple two-layer gravitational edge effect model. Uncertainties based upon the statistical properties of each profile are also determined. A geoid slope-age relation is constructed by normalizing the geoid offsets and uncertainties by the age offsets. The results are in agreement with geoid slope-age relations determined from symmetrically spreading ridges (Sandwell and Schubert, 1980). However, the fracture zone estimates have smaller uncertainties and show less scatter. A comparison of these results with the geoid slope-age prediction of the boundary layer cooling model shows that the thermal structure begins to deviate from this model at an early age (20–40 m.y.). A plate cooling model with a thickness of 125 km is most compatible with the geoid slope-age estimates, although significant deviations occur; these may indicate that the lithospheric thermal structure is not entirely age dependent.

INTRODUCTION

It is generally accepted that the oceanic lithosphere is the surface thermal boundary layer of a mantle convection system [*Oxburgh and Turcotte,* 1978]. According to boundary layer theory [*Turcotte and Oxburgh,* 1967], the cooling and contraction of the oceanic lithosphere as it slides away from the ridge crest results in a surface heat flow which decreases with the age of the crust t as $t^{-1/2}$ and a seafloor depth which increases with crustal age as $t^{1/2}$. Boundary layer theory correctly predicts the observed surface heat flow–age relation for seafloor as old as 110 m.y. [*Lister and Davis,* 1976; *Sclater and Parsons,* 1976; *Parsons and McKenzie,* 1978]. However, the observed depth-age relation begins to flatten from the $t^{1/2}$ law for ages greater than about 70 m.y. [*Parsons and Sclater,* 1977]. This flattening in the average depth-age relation indicates a reduction in boudary layer thickening with age; theory predicts that the surface thermal boundary layer grows in thickness proportionately to $t^{1/2}$. Any mechanism which supplies heat to the base of the lithosphere can retard its rate of cooling and thickening with age. Shear heating in the asthenosphere [*Schubert et al.,* 1976], small-scale convection driven by boundary layer instability [*Richter and Parsons,* 1975], large-scale upwelling due to internal heat sources [*Jarvis and Peltier,* 1980], and lithospheric thinning by hot spots [*Heestand and Crough,* 1981] are all possibilities. The cooling of a constant thickness plate [*McKenzie,* 1967] provides a mathematical model of limited boundary layer growth, although it cannot discriminate among the physical processes that may be responsible for it.

Accurate measurements of the ocean geoid by the GEOS 3 and SEASAT radar altimeters have provided a further constraint on the thermal structure of the cooling lithosphere. Boundary layer theory predicts that geoid height decreases linearly with age with a slope of approximately -0.15 m m.y.$^{-1}$ [*Haxby and Turcotte,* 1978]. This linear decrease in geoid height with age, for ages up to 50 m.y., has been observed on GEOS 3 profiles crossing both the Southwest Indian Ridge [*Chapman,* 1977] and the Mid-Atlantic Ridge [*Haxby and Turcotte,* 1978; *Haxby,* 1979]. For many spreading ridges, however, long-wavelength geoid undulations that are unrelated to lithospheric cooling tend to mask the age-dependent geoid signal. Despite this difficulty the signal can be recovered (albeit with some degree of uncertainty) from geoid height measurements over symmetrically spreading ridges or fracture zones with large age offsets. For symmetrically spreading ridges the portion of the geoid that is related to the age of the lithosphere is symmetric in age about the ridge and invariant along isochrons. By using this a priori knowledge of the properties of the geoid signal associated with lithospheric cooling, *Sandwell and Schubert* [1980] have extracted geoid height-age relations from the observed geoid for large areas in the North Atlantic, South Atlantic, southeast Indian, and southeast Pacific oceans. Except for the southeast Pacific region the data are consistent with the linear decrease predicted by the thermal boundary layer cooling model for ages less than about 80 m.y. For greater ages, however, the observed geoid height-age relations suggested a reduction in the rate of boundary layer thickening with age. In fact these data are also consistent with plate cooling models having thicknesses of about 125 km, as we show later.

An alternate method of extracting the geoid signal associated with lithosphere cooling is to measure the offset in geoid height across a fracture zone [*Crough,* 1979]. Furthermore, if the age offset is known, a geoid height-age relation can be constructed. One advantage of this technique is that the change in geoid height across a fracture zone (FZ) occurs over a relatively short distance (several hundred kilometers). Thus the regional geoid undulations, which are dominant at wavelengths greater than a few thousand kilometers, can be distinguished from the shorter wavelength geoid step. Crough has estimated the geoid step across the Mendocino

[1] Now at the National Geodetic Survey, National Ocean Survey, NOAA, Rockville, Maryland 20852.

Paper number 2B0247.
0148-0227/82/002B-0247$05.00

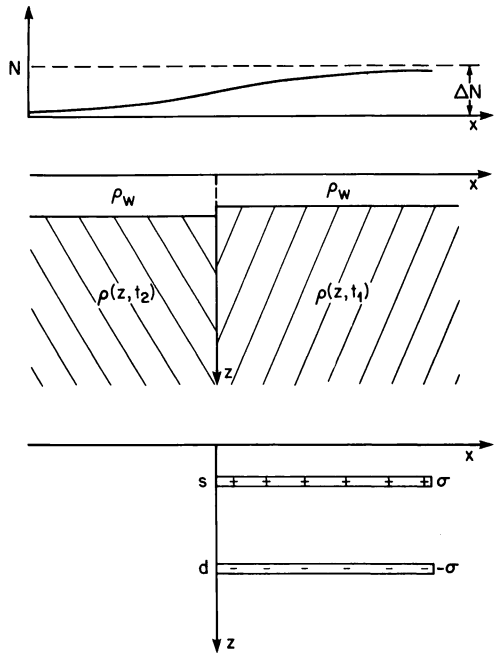

Fig. 1. Gravitational edge effect model used as a fitting function to estimate the overall geoid step. (Top) Smooth step in geoid height associated with two isostatically compensated quarter spaces; ΔN is the geoid offset. (Center) Each quarter space has a density-depth relation that is age dependent. (Bottom) The density contrast across the FZ is approximated by two semi-infinite mass sheets of mass per area σ and $-\sigma$ at depths s and d, respectively.

FZ using GEOS 3 altimeter data and has found that the step estimates are consistent with the thermal boundary layer model if the thermal diffusivity of the lithosphere is 3.3×10^{-7} m^2 s^{-1}. This value of diffusivity is, however, less than one half the value needed to account for the observed depth-age relation. Crough suspected that systematic errors in the estimates of the geoid step may have biased his estimate of the diffusivity. Indeed, the geoid step observed in SEASAT altimeter profiles crossing the younger portion of the Mendocino FZ are well matched by the gravitational edge effect model [*Dorman*, 1975] using the age-dependent thermal structure of the boundary layer cooling model with a more reasonable diffusivity of 8×10^{-7} m^2 s^{-1} [*Sandwell et al.*, 1980]. As pointed out by *Detrick* [1981], the systematic bias in the geoid step estimates made by *Crough* [1979] occurs because the actual geoid step is smooth (i.e., 90% of the step amplitude takes place over a distance of several hundred kilometers), while the fitting function that was used to estimate the step assumes that the entire step takes place over a distance of 200 km [*Crough*, 1979]. By correcting for this bias in the step estimation procedure, *Detrick* [1981] has found that the age variation of the step in the geoid height across the Mendocino FZ is consistent with the prediction of the thermal boundary layer model for ages less than about 30 m.y. At greater ages (30–60 m.y.) however, Detrick's geoid height step estimates are better explained by a plate cooling model with a 100-km-thick lithosphere.

In this study we estimate the geoid height-age relation from SEASAT profiles crossing the Mendocino FZ for ages between 15 and 140 m.y. Rather than estimate the geoid height offset by using the method described by *Crough* [1979], we use a fitting function that more closely approximates the observed smooth steplike variation in the geoid across the fracture zone. The advantages of this technique are that the estimate of the overall step in geoid height is unbiased and the uncertainties in the step estimate truly reflect geoid undulations that are unrelated to the thermogravitational edge effect. In the following sections we discuss the fitting procedure and the geoid height and age data. We then construct the geoid height-age relation and compare it with independently determined estimates [*Sandwell and Schubert*, 1980; *Detrick*, 1981]. Finally, we discuss the implications of the derived geoid height-age relation for thermal models of the oceanic upper mantle.

Theory for Estimating the Geoid Step

The long-wavelength, flat earth approximation [*Ockendon and Turcotte*, 1977] to the geoid of an isostatically compensated cooling lithosphere shows that geoid height depends only upon the age of the lithosphere. While this long wavelength approximation (i.e., the characteristic wavelength of horizontal density variations $\gg 2\pi$ times the average depth of compensation) is valid for the rather smooth lateral changes in density associated with seafloor spreading, it should not be used to model the geoid step across the sharp age and density contrasts at a FZ. Because of the gravitational edge effect [*Dorman*, 1975], geoid height across a FZ is smooth and occurs over a characteristic distance of 2π times the average compensation depth. Thus the overall amplitude of the geoid step can only be determined from the difference between geoid heights far (i.e., $\gg$ 300 km) on either side of the FZ. In theory, this is a valid method of estimating the geoid offset. However, in practice this step measurement technique fails because the smooth FZ geoid signal is generally superimposed upon much larger amplitude geoid undulations that are unrelated to the FZ. This problem can be alleviated somewhat by measuring the geoid offset between two points closer to the FZ (e.g., 100 km on either side of the FZ), in which case the regional geoid will not have as large an effect upon the step estimate. However, only a portion of the step will then be measured. Thus it is apparent that the entire geoid step cannot be observed in the presence of long-wavelength noise (noise in this case is the part of the geoid that is unrelated to the FZ). It is only in the immediate vicinity of the FZ (i.e., within 100 km) that its geoid signal can be unambiguously identified. The overall amplitude of the geoid step must therefore be extrapolated from the small portion of the step that stands out from the regional geoid. This requires the introduction of a FZ model whose parameters are determined from a fit of the model geoid to the observed geoid in the vicinity of the FZ. An extrapolation of the model geoid to distances far from the FZ then provides an estimate of the overall geoid step.

To perform this extrapolation properly, the model must contain the basic characteristics of the FZ density structure. However, it must have only a few adjustable parameters, and the geoid for the model must be easily evaluated so that it is useful as a fitting function. The simple two-layer model shown at the bottom of Figure 1 satisfies these requirements. It is derivable from the more physical model in the middle of the figure, which shows two adjacent isostatically compensated quarter spaces with ages t_1 and t_2 and densities $\rho(z, t_1)$ and $\rho(z, t_2)$ (z is depth). Since we are concerned with the change in geoid height across the FZ, we subtract the density on the left $\rho(z, t_2)$ from the density on both sides. In this new

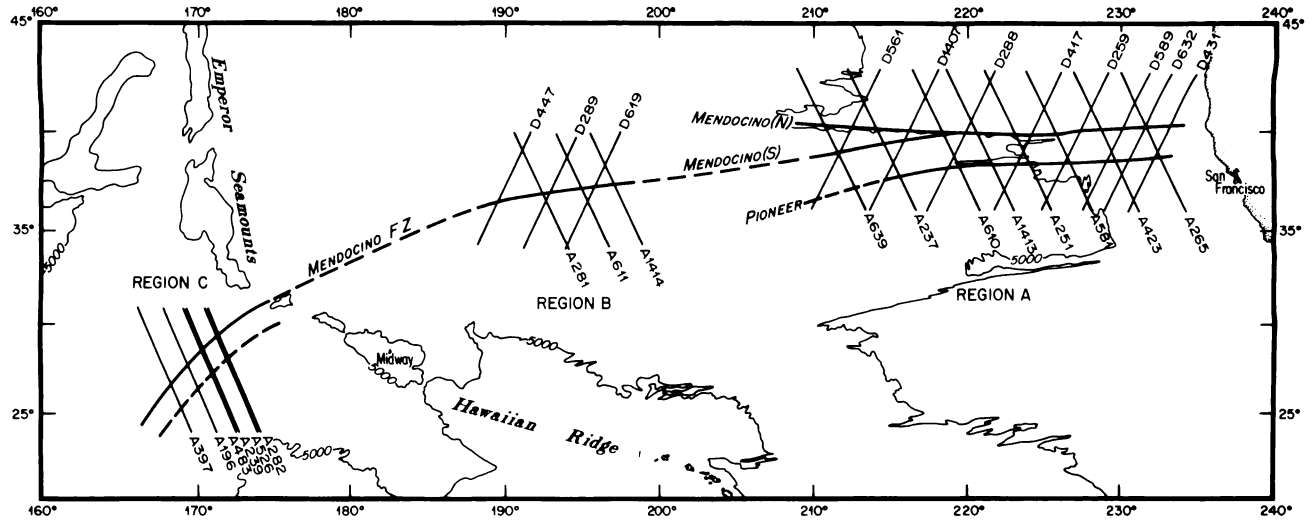

Fig. 2. Location map of the Mendocino FZ. The dashed lines separating regions A, B, and C indicate portions of the FZ that are not readily apparent on bathymetric charts. Seafloor ages on the northern side of the Mendocino FZ increase continuously from 0 m.y. at ~230°E to 140 m.y. at 165°E. Tracks of 28 SEASAT altimeter orbits are labelled by their orbital revolution number and direction: A, ascending and D, descending.

configuration the density on the left side is zero; the largest density contrast on the right side occurs at the average seafloor depth s and is associated with the change in seafloor depth across the FZ. We approximate this horizontal density contrast by a thin sheet with mass per area σ at depth s. The total density contrast at greater depths is represented by a second mass sheet with mass per area $-\sigma$ at the average compensation depth d. Clearly, this two-layer model does not represent the actual lateral density variations across a FZ, since we have compressed the compensating mass into a single sheet and we have ignored the effects of lateral heat conduction [*Louden and Forsyth,* 1976; *Detrick,* 1981] and lithospheric flexure [*Sandwell and Schubert,* 1981]. We will show, however, that good fits to the observed geoid steps can be obtained by varying the two parameters σ and d.

The geoid height N associated with this model is derived in Appendix A; it is given by

$$N(x) = \frac{2\pi G\sigma d}{g}\left\{\frac{1}{2}\left(1 - \frac{s}{d}\right) + \frac{1}{\pi}\left(\arctan\frac{x}{d} - \frac{s}{d}\arctan\frac{x}{s}\right) + \frac{x}{2\pi d}\ln\left(\frac{x^2 + d^2}{x^2 + s^2}\right)\right\} \quad (1)$$

where G is the universal gravitational constant, g is the gravitational acceleration, and x is the horizontal distance from the FZ. The overall geoid step ΔN is derivable from (1) according to

$$\Delta N = \lim_{x\to\infty} N(x) = \frac{2\pi G\sigma}{g}(d - s) \quad (2)$$

We can rewrite (1) in terms of ΔN as

$$N(x) = \Delta N\left[\frac{1}{2} + \left(1 - \frac{s}{d}\right)^{-1}\left\{\frac{1}{\pi}\left(\arctan\frac{x}{d} - \frac{s}{d}\arctan\frac{x}{s}\right) + \frac{x}{2\pi d}\ln\left(\frac{x^2 + d^2}{x^2 + s^2}\right)\right\}\right] \quad (3)$$

The model contains only two adjustable parameters, ΔN and d, because the average seafloor depth s is known.

We will show in the next section that it is preferable to fit the model to the along-track derivative of the observed geoid rather that to the geoid itself because the power spectrum of the geoid slope is nearly white and Gaussian statistics can be used. The geoid slope is

$$\frac{dN}{dx} = \frac{\Delta N}{2\pi(d - s)}\ln\left(\frac{x^2 + d^2}{x^2 + s^2}\right) \quad (4)$$

The form of (4) reveals the role of each of the model parameters. An increase in compensation depth d produces both a broadening in the geoid slope profile and a decrease in its amplitude in such a way that the total area (i.e., the geoid offset) under the geoid slope profile is ΔN. The model is linear in the parameter ΔN, and by design this parameter defines the total geoid offset. In the next section we present the data and use (4) to estimate the geoid offsets for SEASAT altimeter profiles crossing the Mendocino FZ at many locations.

DATA

Location of the Mendocino FZ

The Mendocino FZ in the northeast Pacific was chosen for this geoid age study because of its great horizontal extent and large age offset. As shown in Figure 2, the Mendocino FZ runs continuously from the west coast of North America at 40°N to well beyond the Hawaiian–Emperor Seamount chain at its western extreme. At 220°E it branches into northern and southern extensions. East of 210°E the location of the FZ is defined by the bathymetric scarp on the chart 'Bathymetry of the Northeast Pacific' by *Mammerickx and Smith* [1981]. Between 200°E and 210°E the Mendocino FZ appears quite diffuse, i.e., many parallel scarps exist, as indicated by the dashed line in Figure 2 [*Chase et al.,* 1971]. However, a single scarp which we believe is the western extension of the Mendocino south reappears to the west of 200°E (Region B of Figure 2). To the west of Region B the FZ is again diffuse and sometimes absent in the bathymetric

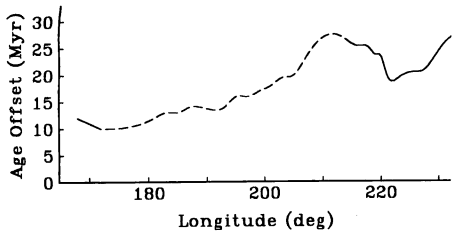

Fig. 3. Age offsets across the Mendocino FZ versus longitude. The age offsets along the solid portions of the curve were determined from dated seafloor magnetic lineations. Along the dashed part of the curve age offsets are derived from a plate reconstruction model.

contours. Along this section it is crosscut by the Hawaiian Swell and the Hawaiian–Emperor Seamount chain. The westernmost segment of the Mendocino FZ is observed in bathymetric contours lying southwest of Midway Island [*Mammerickx*, 1982, Figure 3]. The Pioneer FZ, with a somewhat smaller age offset, lies approximately 150 km to the south of the younger portion of the Mendocino FZ (Region A).

Age Offset along the Mendocino FZ

The age of the Mendocino FZ varies from 0 m.y. at its eastern extreme, where it intersects the Juan de Fuca ridge, to over 130 m.y. at a longitude of 170°E. Magnetic anomalies have been identified in Region A of Figure 2 by *Atwater and Menard* [1970]. We have used the time scale of *Ness et al.* [1980] to date these anomalies and to determine the age offset of the Mendocino FZ as a function of longitude between 210°E and 230°E. Similarly, the Mesozoic magnetic anomalies that have been identified [*Hayes and Pitman*, 1970] and dated [*Larson and Chase*, 1972; *Larson and Pitman*, 1972] in Region C were used to calculate age offset versus longitude along the westernmost portion of the Mendocino FZ. The results are shown by the solid portions of the curve in Figure 3. The age offsets in region B, however, are not well established. We have used the plate reconstruction model of *Larson and Chase* [1972] to infer the longitude dependence of the age offset shown by the dashed curve between 180°E and 210°E in Figure 3. Essentially, age offset increases continuously from 11 m.y. at 180°E to 26 m.y. at 210°E. The age offset curve in Figure 3 is used in the next section, together with estimates of the overall geoid step, to determine the change in geoid height with age.

Geoid Height Profiles across the Mendocino FZ

The locations of 28 SEASAT altimeter profiles that were used to estimate geoid offsets along the Mendocino FZ are shown in Figure 2. We have not used the Seasat profiles that pass over the more diffuse segments of the FZ (dashed lines on Figure 2) because our model assumes that the age and density offsets across the FZ occur at a sharp boundary. The geoid height, which is well approximated by the sea surface height, is shown in Figure 4*a* and *b* for the 11 ascending orbits and 11 descending orbits in regions A and B. In each case the steepest portion of the smooth step in the geoid coincides with the location of the Mendocino FZ. The smaller step at approximately 38.5°N corresponds to the Pioneer FZ. The geoid step associated with the Mendocino FZ in region C is not readily apparent, however, in the geoid profiles shown in Figure 5 (the location of the Mendocino FZ is marked by an arrow on each of the profiles). To enhance the FZ geoid signal with respect to the noise, we have shifted four of these profiles (A239, A483, A196, and A397) so that they line up at the FZ and have made a composite geoid profile by averaging their geoid slopes and integrating the stacked geoid slope profile. This stacked profile, plus a constant, is the uppermost profile in Figure 5. The nearly coincident profiles A282 and A526 were not used to compute the composite geoid profile, since a large seamount at 29.5°N, 173.5°E dominates the FZ geoid signal.

RESULTS

It is apparent from the profiles shown in Figures 4 and 5 that the smooth step associated with the Mendocino FZ is superimposed upon both longer wavelength regional geoid undulations and shorter wavelength geoid variations (noise).

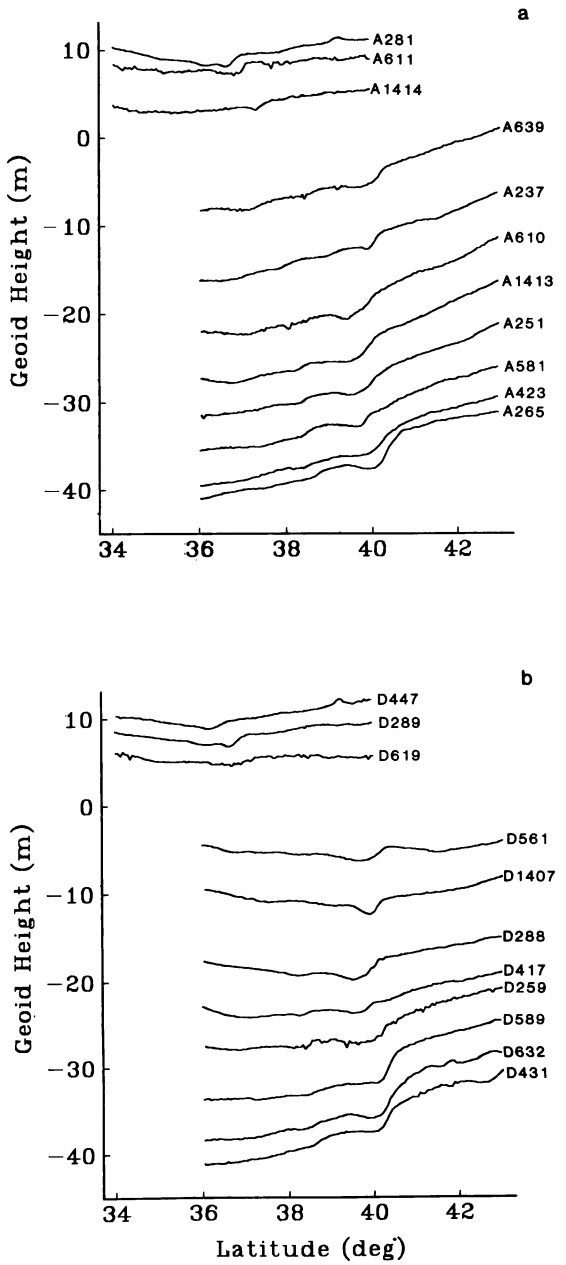

Fig. 4. Relative geoid heights along the orbital tracks of Regions A and B for (*a*) ascending orbits and (*b*) descending orbits. A smooth step in the geoid height occurs at the Mendocino FZ.

The regional geoid can be modelled by a second-order polynomial [*Crough*, 1979], but the shorter wavelength noise cannot be directly separated from the FZ geoid signal. Instead, the best estimate of the overall geoid offset is found by varying the model parameters ΔN and d and the parameters of the quadratic fit to the regional geoid until the rms of the residuals between the model and the data is minimized. This least squares fitting procedure requires that the residuals have a Gaussian distribution or, alternatively, that the power spectrum of the residuals is white. However, after fitting a geoid profile using this procedure we found that the power spectrum of the residuals was red, i.e., it decreased with increasing wavenumber k according to k^{-2}. We therefore prewhitened the noise spectrum by taking the along-track derivative of the geoid profile (an example is given in Figure 6). This technique not only whitens the noise spectrum but also has other advantages. First, the derivative of the regional geoid representation has one less parameter. Second, the FZ geoid signal dominates the geoid slope whereas it is a minor component of the geoid. Thus more emphasis is placed upon minimizing the residuals in the vicinity (within 100 km) of the FZ rather than those far from the FZ. Finally, the peak in the geoid slope clearly delineates the FZ and can be used to locate it in areas where bathymetric data are unavailable.

The overall geoid offset for each of the profiles was estimated by minimizing the sum of the squares of the differences between the observed geoid slope and the model geoid slope

$$\frac{dN}{dx} = ax + b + \frac{\Delta N}{2\pi(d - s)} \ln\left(\frac{(x - x_0)^2 + d^2}{(x - x_0)^2 + s^2}\right) \quad (5)$$

where a and b specify the slope and intercept of the derivative of the regional geoid and x_0 is the location of the FZ. We included an additional term for the profiles in region A to account for the effect of the geoid step at the Pioneer FZ on the Mendocino FZ geoid signal. The parameter estimation problem is linear in all of the model parameters except for x_0 and d. The best set of model parameters was determined by using an iterative nonlinear technique due to *Marquardt* [1963]. In general, the algorithm required two iterations to converge, and the final set of model parameters

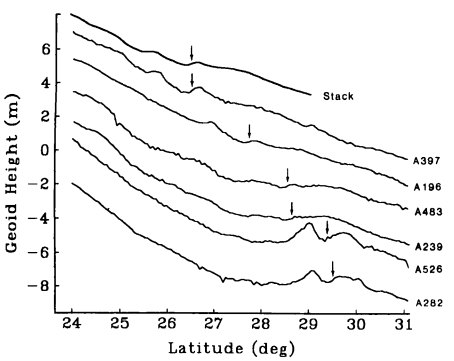

Fig. 5. Relative geoid height profiles from Region C. The location of the Mendocino FZ, determined from bathymetric contours [*Mammerickx*, 1982], is marked by an arrow on each profile. The FZ geoid step is not readily apparent on these profiles. To enhance the FZ geoid signal, the profiles A239, A483, A196 and A397 were aligned at the arrows and stacked to yield the profile shown at the top. Profiles A526 and A282 were not used because of the seamount near the FZ.

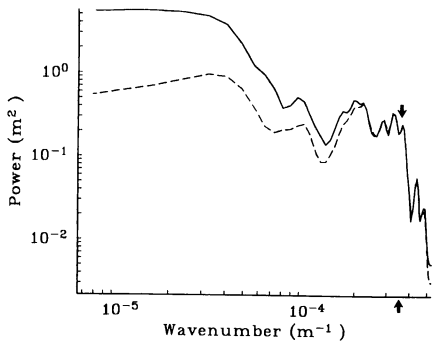

Fig. 6. Power spectrum of the along track derivative of the geoid profile A423 (solid curve). The dashed curve represents the power spectrum after the best fitting model was removed. This spectrum is nearly 'white' for wavenumbers less than the corner wavenumber marked by the arrow at 2.6×10^{-4} m^{-1}. The spectra were smoothed for presentation.

was insensitive to the starting model. However, profiles A251 and D417, which pass over the same part of the Mendocino FZ, and individual profiles in Region C required special attention. For profiles A251 and D417, satisfactory results, i.e. nonnegative compensation depths d, were obtained by choosing a different starting model. Problems arose in fitting the model to the individual profiles in Region C because the FZ geoid signal is smaller than the noise. The signal was boosted to roughly twice the noise level by stacking four of the geoid profiles, as described earlier.

An uncertainty estimate for each of the model parameters was calculated from a linear approximation to the model in the neighborhood of the best set of model parameters. The uncertainty estimate is highly dependent upon the number of degrees of freedom in the geoid slope profile. For a white noise spectrum that has a corner wavenumber (i.e., the power spectrum falls rapidly at higher wavenumbers) of

$$k_{cor} = \frac{2\pi}{\lambda_{cor}}$$

the number of degrees of freedom is

$$(n - p)\ \lambda_{min}/\lambda_{cor}$$

where n is the number of data points in the profile, p is the number of model parameters, and λ_{min} is twice the distance between data points. Figure 6 shows the power spectrum of the geoid slope (solid line) and the residual geoid slope (dashed line) for profile A423. The residual power spectrum is nearly white for wavenumbers between 8×10^{-6} m^{-1} and 3×10^{-4} m^{-1}. At higher wavenumbers the power declines rapidly. This corner wavenumber is shown by an arrow in Figure 6; λ_{cor} has a value of 21 km.

Examples of model fits to observed geoid profiles from regions A, B, and C and their associated residuals are shown in Figure 7. In every case the model (5) was fit to the along-track derivative of the profile. The fit to the geoid height was obtained by integrating the model. In general, the rms of the residual geoid is less than 0.5 m. Twenty out of 22 profiles from regions A and B have a geoid slope with a component which is antisymmetric about the Mendocino FZ. For ascending orbits the geoid slope is depressed on the older side of the FZ. Similarly, the descending orbits show elevated geoid slopes on the older side. This antisymmetric component cannot be fit by (5) because the gravitational edge effect

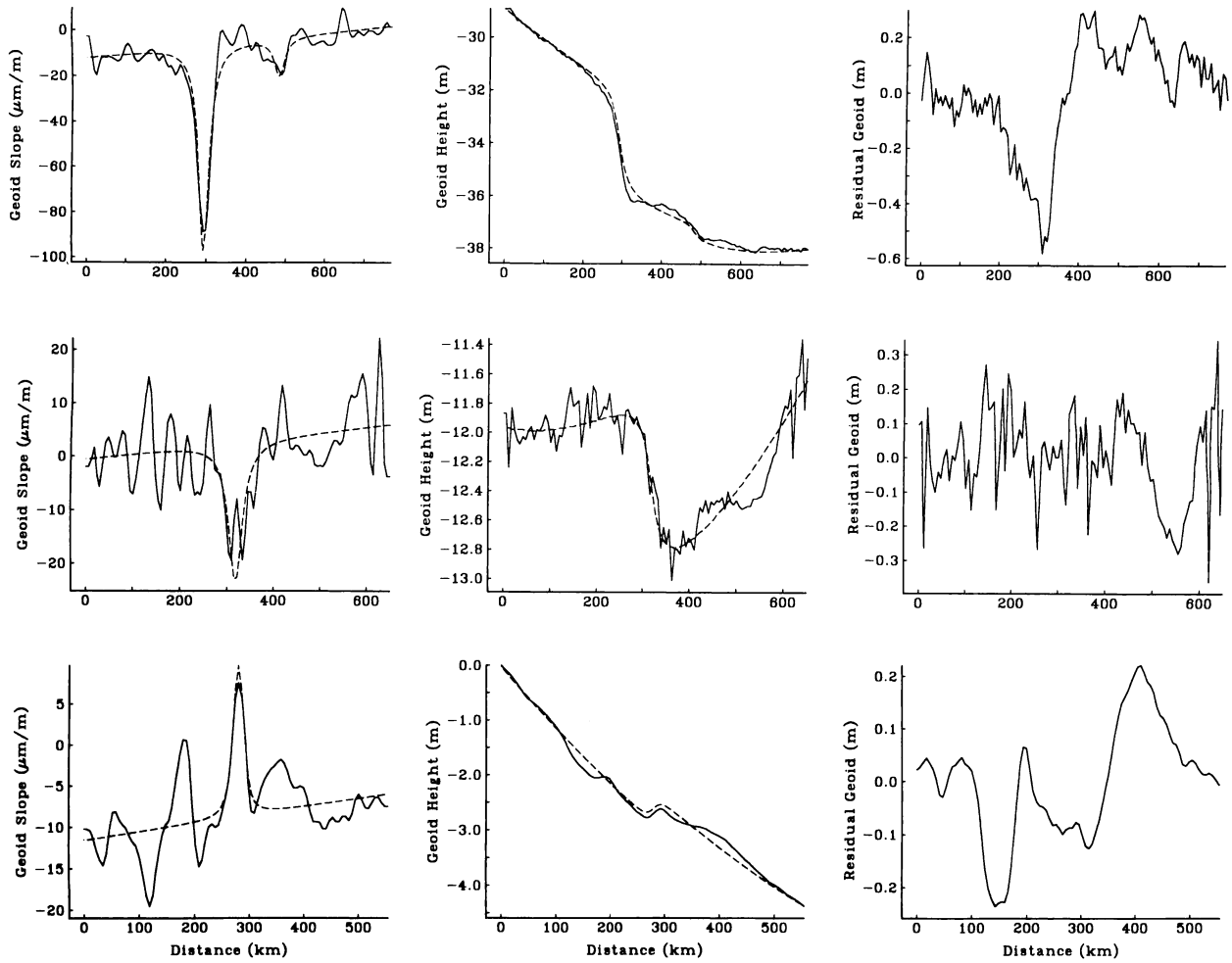

Fig. 7. Best fitting models to profiles from Region A (D589), Region B(D619), and Region C (stacked profile) are shown in the upper, middle, and lower rows, respectively. The parameters of the model (5) were varied in a least squares fit to the along track derivative of the geoid shown in the left column (filtered for presentation with a 16-km-half-width Gaussian filter). The integral of the model plus a constant and the observed geoid profile are shown in the center column. The residual geoid height is plotted on the right and has typical values of ±0.3 m.

predicts a geoid slope that is symmetric about the FZ. The asymmetry may be a result of flexure at the FZ caused by the difference in subsidence rates on either side of the FZ together with the difference in age-dependent flexural rigidities across the FZ [*Sandwell and Schubert,* 1981].

A complete summary of the estimated geoid offsets and their uncertainties, the depths of compensation d and their uncertainties, the age offsets Δt, the average ages t_{ave}, and the changes in geoid height divided by the associated age offsets is given in Table 1. The estimates of the overall geoid offset ΔN divided by the age offset Δt and associated uncertainties are plotted against the average age of the two lithospheric segments in Figure 8. For ages less than about 20 m.y. the geoid slope is slightly greater than −0.15 m m.y.$^{-1}$, while for greater ages it is between −0.05 and −0.10 m m.y.$^{-1}$. In the next section we compare this geoid slope-age relation with independently determined estimates. We then discuss all of the data in terms of lithospheric cooling models.

Discussion

The overall geoid steps for 18 SEASAT altimeter profiles crossing the Mendocino FZ have recently been estimated by *Detrick* [1981]. Many of the profiles used in his study either intersect the profiles we have chosen or are identical to ours. However, different methods were used in the two studies to estimate the geoid step. To compare our results with Detrick's, we have corrected his estimates for the bias introduced by his measurement procedure (using his bias model, Figure 8 of *Detrick* [1981]) and averaged his estimates over 10-m.y. time intervals. We have also averaged our estimates, weighted by their uncertainties, over the same 10-m.y. age intervals. Both sets of results are shown in Figure 9, where the asterisks represent Detrick's estimates and the octagons represent our points. The agreement is quite good, considering that more than half of our profiles were taken from different orbits than Detrick's. The major difference between the two studies lies in the data selection at ages greater than 60 m.y. We did not use the profiles crossing the Mendocino FZ between ages of 60 and 80 m.y. since this portion of the FZ is not clearly delineated in the bathymetric contours [*Chase et al.,* 1971]. In addition, we have estimated $\Delta N/\Delta t$ at 88 and 135 m.y., although the formal uncertainty in the 88 m.y. estimate may not reflect the actual uncertainty because the age offset in this region is only poorly constrained. The good agreement between the two data sets at young ages

TABLE 1. Age, Age Offset, Geoid Offset and Change in Geoid Height With Age Offset for Profiles Crossing the Mendocino FZ

Orbit Number	t_{ave}, m.y.	Δt, m.y.	$\Delta N \pm \sigma_{\Delta N}$, m	$\Delta N/\Delta t \pm \sigma_{\Delta N/\Delta t}$ m m.y.$^{-1}$	$d \pm \sigma_d$, km
			Region A		
A265	15.6	−26.9	4.84 ± 0.86	−0.179 ± 0.032	36.3 ± 10.4
D431*	16.0	22.0	−3.28 ± 0.68	−0.149 ± 0.031	18.4 ± 10.3
D632	16.1	26.8	−5.13 ± 1.16	−0.191 ± 0.051	39.1 ± 18.0
D589	19.3	24.3	−4.53 ± 0.52	−0.186 ± 0.025	29.0 ± 7.0
A423	22.4	−22.5	3.44 ± 0.75	−0.155 ± 0.034	49.5 ± 16.2
D259	27.4	21.7	−3.44 ± 1.10	−0.158 ± 0.060	39.4 ± 24.5
A581	29.0	−20.5	2.82 ± 2.10	−0.138 ± 0.101	104.1 ± 89.8
D417	32.0	20.0	−2.44 ± 1.23	−0.122 ± 0.063	59.8 ± 28.4
A251	34.2	−19.2	2.33 ± 0.73	−0.114 ± 0.042	33.7 ± 21.0
A1413	39.1	−22.6	2.92 ± 0.78	−0.129 ± 0.041	34.6 ± 19.3
D288	40.6	23.5	−3.36 ± 0.66	−0.143 ± 0.033	37.6 ± 14.8
A610	43.0	−24.8	3.07 ± 1.03	−0.124 ± 0.049	44.6 ± 27.4
D1407	46.3	25.4	−1.84 ± 0.30	−0.072 ± 0.014	9.6 ± 12.6
A237	50.0	−26.4	2.19 ± 0.57	−0.083 ± 0.022	15.6 ± 11.8
D561	55.0	26.0	−1.92 ± 0.59	−0.074 ± 0.023	19.6 ± 17.0
A639	60.3	25.4	2.18 ± 0.49	−0.086 ± 0.023	19.6 ± 11.2
			Region B		
A1414	84.0	−16.0	1.12 ± 0.469	−0.070 ± 0.035	11.1 ± 21.5
D619	85.4	16.0	−1.51 ± 0.303	−0.094 ± 0.023	32.4 ± 9.4
A611	86.0	−16.0	1.12 ± 0.409	−0.070 ± 0.030	9.4 ± 9.9
D289	88.2	14.0	−1.61 ± 0.387	−0.115 ± 0.033	13.0 ± 10.2
A281	88.8	−13.8	1.61 ± 0.456	−0.117 ± 0.033	12.1 ± 13.1
D447	91.7	13.5	−1.15 ± 0.429	−0.085 ± 0.038	19.0 ± 12.4
			Region C		
A239 + A483 + A196 + A397	133.3	−11.3	0.59 ± 0.362	−0.052 ± 0.032	8.4 ± 7.6

*This profile intersects the Mendocino FZ to the east of the Juan de Fuca spreading ridge and therefore it has a smaller offset than adjacent profiles.

lends additional support to the validity of our estimates at 88 and 135 m.y. even though these two points do not lie along the general trend of the other points.

Further comparisons can be made with the estimated geoid slope-age relations for symmetrically spreading ridges [*Sandwell and Schubert,* 1980]. Figure 9 also shows estimates and uncertainties of the geoid slope for the North Atlantic south of 32°N, the South Atlantic, and the southeast Indian Ocean areas [*Sandwell and Schubert,* 1980]. In general, our estimates from these three oceanic areas are consistent with the FZ estimates; however, the FZ data have smaller uncertainties and show less scatter. These smaller uncertainties allow us to discriminate among the various lithospheric cooling models. The boundary layer cooling model predicts that the geoid slope remains constant for all ages; a value of −0.15 m m.y.$^{-1}$ has been estimated by *Haxby and Turcotte* [1978]. The results from the symmetrically spreading ridges are consistent with a constant geoid slope for ages less than 80 m.y. The more accurate FZ geoid slope estimates, however, are consistent with the boundary layer model only for ages less than about 40 m.y. Figure 9 also shows geoid slope-age relations for plate cooling models [*Sandwell and Schubert,* 1980; *Parsons and Richter,* 1980]. The values of the thermal parameters used in these model calculations are from the best-fitting plate model of the depth-age relation in the North Pacific [*Parsons and Sclater,* 1977]: thermal expansion coefficient = 3.3×10^{-5} K^{-1}, temperature contrast across the plate = 1330 K, thermal diffusivity = 8×10^{-7} m^2 s^{-1}. Theoretical geoid slope-age relations for plate thicknesses of 200 km (dashed curves), 125 km (solid curves), and 100 km (dotted curves) illustrate the sensitivity of the relation to this parameter. Values of plate thickness between about 100 and 125 km are most consistent with all of the geoid slope estimates. Because the uncertainties in the geoid slope estimates for the symmetrically spreading ridges are relatively large, these data are also consistent with a plate thickness of 200 km, which gives a flattening in the geoid height-age relation at 80 m.y. However, this value of plate thickeness is incompatible with the FZ geoid slope estimates.

For completeness we have also compared the depth to the compensating mass, averaged over 10 m.y. are intervals, with the average depth of compensation predicted by the plate cooling model (see Appendix B) for plate thicknesses of 100, 125, and 200 km. These results are shown in Figure 10. For ages less than about 30 m.y., the agreement between the models and the data is quite good. However, for greater ages all the plate model compensation depths deviate significantly from the observations. The parameter d reflects the sharpness of the geoid step, i.e., larger d imply broader geoid

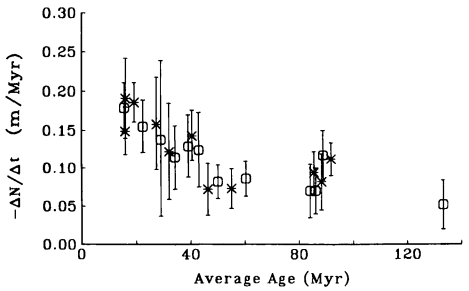

Fig. 8. Geoid slope estimates and uncertainties for profiles shown in Figures 4 and 5 determined by normalizing the geoid offsets by the age offsets. These are plotted against the average age across the FZ. Octagons indicate ascending orbits; asterisks, descending orbits.

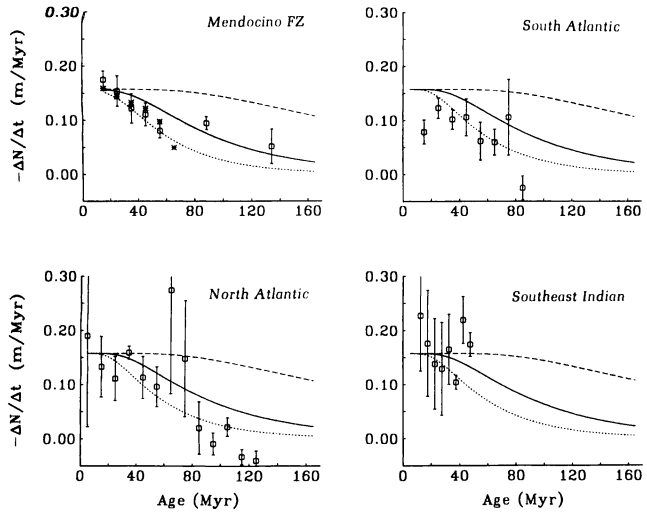

Fig. 9. Geoid slope-age estimates averaged over 10-m.y. age intervals for the Mendocino FZ, the North Atlantic south of 32°N, and the South Atlantic. The estimates for the Southeast Indian Ocean were averaged over 5-m.y. age intervals (octagons). Asterisks represent Mendocino FZ geoid slope-age estimates from *Detrick* [1981]. Symmetric spreading ridge data are from *Sandwell and Schubert* [1980]. Also shown are geoid slope-age relations predicted by plate cooling models with plate thicknesses of 100 km (dotted curve), 125 km (solid curve), and 200 km (dashed curve).

steps. The observed decrease in d with age between ages of 30 and 130 m.y. indicates that the geoid step becomes sharper with age. The thermogravitational edge effect model predicts, however, that the geoid step broadens with age. Although we do not fully understand this discrepancy between the observed and model d, we believe that our estimates of the amplitudes of the overall geoid steps are unaffected by their widths.

The geoid slope-age relation is much more sensitive to the thickness of the lithosphere than are the depth-age and heat flow–age relations. To demonstrate this, the heat flow–age relation for well-sedimented seafloor throughout the oceans [*Sclater et al.*, 1980], the depth-age relation for the North Atlantic south of 35°N [*Parsons and Sclater*, 1977], and the depth-age relation for the North Pacific [*Sclater et al.*, 1971; *Parsons and Sclater*, 1977] are shown in Figure 11 together with the predictions of the plate cooling models using the same parameter values as in Figure 9. The heat flow–age relation is notably insensitive to the lithospheric thickness, while the depth-age relation is moderately sensitive to this parameter. In contrast, the geoid slope-age relation changes by more than an order of magnitude at 160 m.y. when the lithospheric thickness is changed from 100 to 200 km. Thus small changes in the thermal structure near the base of the lithosphere produce large changes in the geoid slope for ages greater than about 40 m.y.

A better understanding of the enhanced sensitivity of the geoid slope to thermal perturbations in the lower portion of the lithosphere comes directly from the long-wavelength, flat earth approximation to the geoid height for isostatically compensated topography [*Ockendon and Turcote*, 1977]

$$N(x) = \frac{-2\pi G}{g} \int_0^\infty \rho(x, z)\, z\, dz \qquad (6)$$

Seafloor depth is proportional to

$$\int_0^\infty \rho(x, z)\, dz$$

It is apparent from these equations that density variations at depth have more effect upon the geoid than the seafloor elevation simply because of the weighting function z in the integrand.

Based upon the data and models presented in Figures 9 and 11, we believe that the average lithospheric thermal structure is best approximated by a plate cooling model with a 125-km-thick plate. A plate model with 100-km thickness does not fit the geoid slope-age estimates from the Mendocino FZ at 88 and 135 m.y., and it also does not fit the North Pacific depth-age data for ages greater than 40 m.y. A thick plate model (200 km) shows a generally poor fit to all but the heat flow data. In contrast the predictions of the 125-km-thick plate model are in good agreement with the depth-age and heat flow–age data [*Parsons and Sclater*, 1977] and provide the best overall fit to the Mendocino geoid slope-age estimates.

Although on the average the 125-km-thick plate model has the best fit to all of the data, it does not fit the Mendocino geoid slope estimates in detail. A 100-km-thick plate model provides a better fit to these estimates between 15 and 60 m.y., while a 140-km-thick plate model better fits the estimates at greater ages. This same effect occurs with the North Pacific seafloor depths, although these deviations are hidden in Figure 11 by averaging seafloor depths along isochrons. The North Pacific contains large areas of seafloor that are either shallower or deeper than the average depth-age relation [*Menard*, 1973; *Mammerickx*, 1982]. Such broad residual depth anomalies have been explained by age independent heat inputs into the base of the lithosphere, i.e., lithospheric heating [*Heestand and Crough*, 1981]. By averaging along isochrons, the average depth-age relation is extracted and the residual depth anomalies are reflected in the uncertainties.

In this study we have sampled only a small portion of the seafloor that is adjacent to the Mendocino FZ. Therefore, our geoid slope-age estimates may not represent the average geoid slope-age relation in the North Pacific. Furthermore, we have shown that these estimates are very sensitive to the

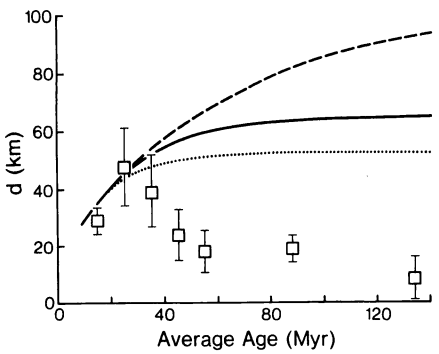

Fig. 10. Estimates of average compensation depth d versus average age across the Mendocino FZ (octagons). Error bars represent linearized one standard deviation uncertainties. Curves are predicted average compensation depths for the plate cooling model with plate thicknesses of 100 km (dotted line), 125 km (dashed line), and 200 km (dashed line).

thermal structure of the lowermost portion of the lithosphere. It appears that the significant departures (Figure 9) in the geoid slope-age estimates from the 125-km-thick plate model are reflecting deviations in the thermal structure along the Mendocino FZ from the plate cooling model. Obviously, this occurs along the portion of the Mendocino FZ that is crosscut by the Hawaiian swell, since the FZ geoid signal is absent in this region. In addition, smaller reheating anomalies that have intersected other segments of the Mendocino FZ will also erase a portion of the FZ geoid signal. The enhanced sensitivity of the geoid height to thermal perturbations near the base of the lithosphere makes *this data set* very useful for mapping lithospheric reheating anomalies.

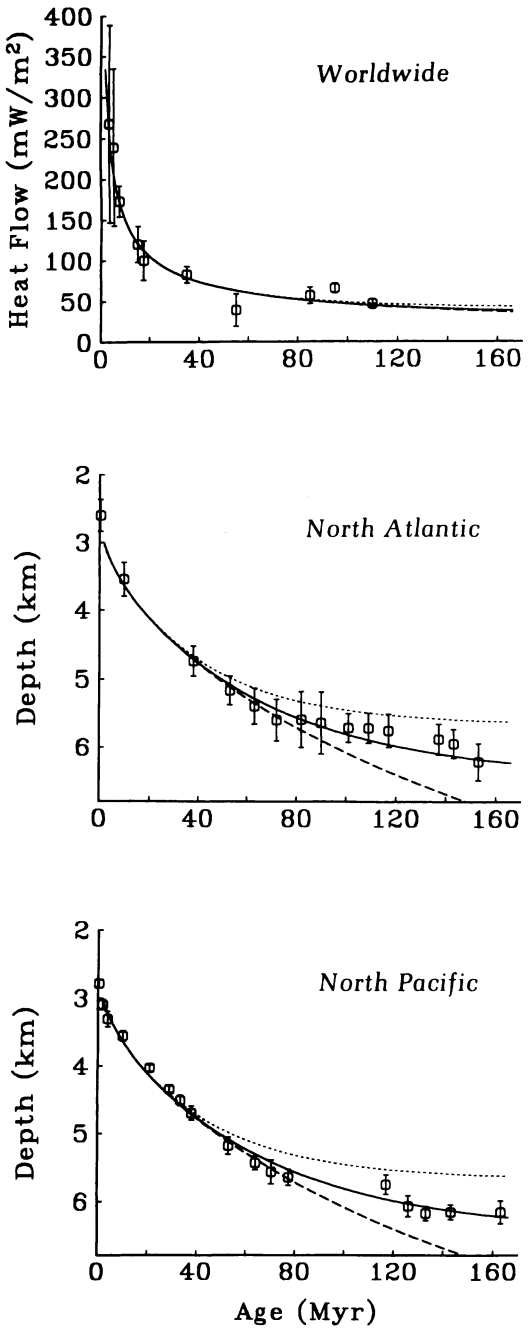

Fig. 11. Heat flow–age relation (top) for well-sedimented seafloor throughout the oceans [*Sclater et al.*, 1980] and depth-age relations for the North Atlantic (middle) and the North Pacific (bottom) [*Sclater et al.*, 1971; *Parsons and Sclater*, 1977]. Curves are predictions of the plate cooling model for plate thicknesses of 100 km (dotted), 125 km (solid), and 200 km (dashed).

Appendix A: A Simple Fracture Zone Model

The geometry of the two-layer FZ model [*Dorman*, 1975] is shown in Figure 1. The gravitational potential U is produced by two semi-infinite sheets of mass with mass per unit area σ and $-\sigma$ at depths s and d beneath the observation plane. The potential U is the three-dimensional convolution of the density structure ρ with the Green's function due to a point mass:

$$U(\mathbf{r}) = \int \rho(\mathbf{r}_0) \frac{G}{|\mathbf{r} - \mathbf{r}_0|} dV_0 \qquad \text{(A1)}$$

where $\mathbf{r}_0$ is the position vector of the source, $\mathbf{r}$ is the location of the observer, dV_0 is the element of volume at $\mathbf{r}_0$, and the integration extends over all space. Upon integrating over z_0 from $-\infty$ to $+\infty$ and over y_0 from $-L$ to L, we find

$$U(x, 0, 0) = G\sigma \int_0^\infty \ln \left[\frac{L + (L^2 + a_1^2)^{1/2}}{-L + (L^2 + a_1^2)^{1/2}} \cdot \frac{-L + (L^2 + a_2^2)^{1/2}}{L + (L^2 + a_2^2)^{1/2}} \right] dx_0 \qquad \text{(A2)}$$

where

$$a_1^2 = (x - x_0)^2 + s^2 \qquad a_2^2 = (x - x_0)^2 + d^2 \qquad \text{(A3)}$$

In the limit $L \to \infty$, (A2) becomes

$$U(x) = G\sigma \int_0^\infty \ln \left(\frac{(x - x_0)^2 + d^2}{(x - x_0)^2 + s^2} \right) dx_0$$

$$= 2\pi G\sigma d \left\{ \frac{1}{2} \left(1 - \frac{s}{d} \right) + \frac{1}{\pi} \left(\arctan \frac{x}{d} - \frac{s}{d} \arctan \frac{x}{s} \right) + \frac{x}{2\pi d} \ln \left(\frac{x^2 + d^2}{x^2 + s^2} \right) \right\} \qquad \text{(A4)}$$

To first order the geoid height N is U/g. It is noteworthy that the potential for this model is undefined, on a flat earth, if the densities of the mass layers are not equal and opposite (the requirement of isostatic compensation). The slope of the potential, which is used in our fitting procedure, is

$$\frac{dU}{dx} = G\sigma \ln \left(\frac{x^2 + d^2}{x^2 + s^2} \right) \qquad \text{(A5)}$$

Appendix B: Average Compensation Depth for the Plate Cooling Model

The mass per unit area σ corresponding to the change in depth across the FZ is the depth offset multiplied by the seafloor-seawater density contrast. For the plate cooling model [*McKenzie*, 1967], σ is

$$\sigma = \{\rho_m + \alpha\rho_m(T_m - T_0) - \rho_w\}\{D(t_2) - D(t_1)\} \qquad \text{(B1)}$$

where ρ_m is the mantle density, α is the coefficient of thermal expansion, $(T_m - T_0)$ is the temperature contrast across the

plate, ρ_w is the seawater density, and $D(t)$ is the depth-age relation. The geoid offset across the FZ, given in (2), is

$$N(t_1) - N(t_2) = \frac{2\pi G\sigma}{g}(d - s) \tag{B2}$$

where $N(t)$ is the geoid height-age relation. By eliminating σ from equations (B1) and (B2), we find that the average compensation depth d is

$$d = \frac{g}{2\pi G\{\rho_m + \alpha\rho_m(T_m - T_0) - \rho_w\}}\left(\frac{N(t_1) - N(t_2)}{D(t_2) - D(t_1)}\right) + s \tag{B3}$$

Acknowledgments. We thank Russell Agreen for providing many of the SEASAT altimeter profiles and LeRoy Dorman for helpful suggestions. This work was supported by the NASA Geodynamics Program under grant NAG 5152.

REFERENCES

Atwater, T., and H. W. Menard, Magnetic lineations in the northeast Pacific, *Earth Planet. Sci. Lett., 7,* 445–450, 1970.

Chapman, M. E., Geoid anomaly over midocean ridges (abstract), *Eos Trans. AGU, 58,* 368, 1977.

Chase, T. E., H. W. Menard, and J. Mammerickx, Topography of the North Pacific chart TR-17; La Jolla Inst. of Mar. Resour., Univ. of Calif., San Diego, 1971.

Crough, S. T., Geoid anomalies across fracture zones and the thickness of the lithosphere, *Earth Planet. Sci. Lett., 44,* 224–230, 1979.

Detrick, R. S., Jr., An analysis of geoid anomalies across the Mendocino fracture zone: Implications for thermal models of the lithosphere, *J. Geophys. Res., 86,* 11, 751, 1981.

Dorman, L. M., The gravitational edge effect, *J. Geophys. Res., 80,* 2949–2950, 1975.

Haxby, W. F., The mid-ocean ridge geoid anomaly (abstract), *Eos Trans. AGU, 60,* 391, 1979.

Haxby, W. F., and D. L. Turcotte, On isostatic geoid anomalies, *J. Geophys. Res., 83,* 5473–5478, 1978.

Hayes, D. E., and W. C. Pitman, Magnetic lineations in the North Pacific, *Geol. Soc. America Mem., 126,* 291–314, 1970.

Heestand, R. L., and S. T. Crough, The effect of hot spots on the oceanic age-depth relation, *J. Geophys. Res., 86,* 6107–6114, 1981.

Jarvis, G. T., and W. R. Peltier, Flattening of ocean bathymetry profiles due to radiogenic heating in a convecting mantle, *Nature, 285,* 649–651, 1980.

Larson, R. L., and C. G. Chase, Late Mesozoic evolution of the western Pacific Ocean, *Geol. Soc. Am. Bull., 83,* 3627–3643, 1972.

Larson, R. L., and W. C. Pitman III, World-wide correlation of Mesozoic magnetic anomalies, and its implications, *Geol. Soc. Am. Bull., 83,* 3645–3662, 1972.

Lister, C. R. B., and E. E. Davis, Comments on 'Comparison of long-wavelength residual elevation and free air gravity anomalies in the North Atlantic and possible implications for the thickness of the lithospheric plate' by John G. Sclater, Lawrence A. Lawver, and Barry Parsons, *J. Geophys. Res., 81,* 4957–4959, 1976.

Louden, K. E., and D. W. Forsyth, Thermal conduction across fracture zones and the gravitational edge effect, *J. Geophys. Res., 81,* 4869–4874, 1976.

Mammerickx, J., Depth anomalies over Mesozoic crust in the western Pacific, *Geodyn. Ser.,* AGU, in press, 1982.

Mammerickx, J., and S. M. Smith, Bathymetry of the Northeast Pacific, *Map and Chart Ser. MC-43,* Geol. Soc. of Am., 1981.

Marquardt, D. L., An algorithm for least-squares estimation of nonlinear parameters, *J. Soc. Ind. Appl. Math., 2,* 431–441, 1963.

McKenzie, D. P., Some remarks on heat flow and gravity anomalies, *J. Geophys. Res., 72,* 6261–6273, 1967.

Menard, H. W., Depth anomalies and the bobbing motion of drifting islands, *J. Geophys. Res., 78,* 5128–5137, 1973.

Ness, G., S. Levi, and R. Couch, Marine magnetic anomaly timescales for the Cenozoic and late Cretaceous: A précis, critique, and synthesis, *Rev. Geophys. Space Phys., 18,* 753–770, 1980.

Ockendon, J. R., and D. L. Turcotte, On the gravitational potential and field anomalies due to thin mass layers, *Geophys. J. Roy. Astron. Soc., 48,* 479–492, 1977.

Oxburgh, E. R., and D. L. Turcotte, Mechanisms of continental drift, *Rep. Prog. Phys., 41,* 1249–1312, 1978.

Parsons, B., and D. P. McKenzie, Mantle convection and the thermal structure of the plates, *J. Geophys. Res., 83,* 4485–4496, 1978.

Parsons, B., and F. M. Richter, A relation between driving forces and geoid anomaly associated with mid-ocean ridges, *Earth Planet. Sci. Lett., 51,* 445–450, 1980.

Parsons, B., and J. G. Sclater, An analysis of the variation of ocean floor bathymetry and heat flow with age, *J. Geophys. Res., 82,* 803–827, 1977.

Richter, F. M., and B. Parsons, On the interaction of the two scales of convection in the mantle, *J. Geophys. Res., 80,* 2529–2541, 1975.

Sandwell, D., and G. Schubert, Geoid height versus age for symmetric spreading ridges, *J. Geophys. Res., 85,* 7235–7241, 1980.

Sandwell, D., and G. Schulbert, Lithospheric flexure at fracture zones, *J. Geophys. Res.,* in press, 1981.

Sandwell, D. T., G. Schubert, and R. V. Sailor, Geoid height across fracture zones (abstract), *Eos Trans. AGU, 61,* 1123, 1980.

Schubert, G., C. Froidevaux, and D. A. Yuen, Oceanic lithosphere and asthenosphere: Thermal and mechanical structure, *J. Geophys. Res., 81,* 3525–3540, 1976.

Sclater, J. G., and B. Parsons, Reply, *J. Geophys. Res., 81,* 4960–4964, 1976.

Sclater, J. G., R. N. Anderson, and M. L. Bell, Elevation of ridges and evolution of the central eastern Pacific, *J. Geophys. Res., 76,* 7888–7915, 1971.

Sclater, J. G., C. Jaupart, and D. Galson, The heat flow through oceanic and continental crust and the heat loss of the earth, *Rev. Geophys. Space Phys., 18,* 269–311, 1980.

Turcotte, D. L., and E. R. Oxburgh, Finite amplitude convective cells and continental drift, *J. Fluid Mech., 28,* 24–42, 1967.

(Received September 28, 1981;
revised February 1, 1982;
accepted February 10, 1982.)